MATERIALS SCIENCE

10.1126/sciadv.1501814

Giant electromechanical coupling of relaxor ferroelectrics controlled by polar nanoregion vibrations

Michael E. Manley,[1]* Douglas L. Abernathy,[2] Raffi Sahul,[3†] Daniel E. Parshall,[4] Jeffrey W. Lynn,[4] Andrew D. Christianson,[2] Paul J. Stonaha,[1] Eliot D. Specht,[1] John D. Budai[1]

Relaxor-based ferroelectrics are prized for their giant electromechanical coupling and have revolutionized sensor and ultrasound applications. A long-standing challenge for piezoelectric materials has been to understand how these ultrahigh electromechanical responses occur when the polar atomic displacements underlying the response are partially broken into polar nanoregions (PNRs) in relaxor-based ferroelectrics. Given the complex inhomogeneous nanostructure of these materials, it has generally been assumed that this enhanced response must involve complicated interactions. By using neutron scattering measurements of lattice dynamics and local structure, we show that the vibrational modes of the PNRs enable giant coupling by softening the underlying macrodomain polarization rotations in relaxor-based ferroelectric PMN-*x*PT {$(1-x)[Pb(Mg_{1/3}Nb_{2/3})O_3] - xPbTiO_3$} ($x$ = 30%). The mechanism involves the collective motion of the PNRs with transverse acoustic phonons and results in two hybrid modes, one softer and one stiffer than the bare acoustic phonon. The softer mode is the origin of macroscopic shear softening. Furthermore, a PNR mode and a component of the local structure align in an electric field; this further enhances shear softening, revealing a way to tune the ultrahigh piezoelectric response by engineering elastic shear softening.

INTRODUCTION

Understanding how inhomogeneous nanoregions enhance functional properties is an outstanding scientific challenge for a broad class of materials that includes not only relaxor ferroelectrics (*1*) but also superelastic strain glass shape-memory alloys (*2*), colossal magnetoresistance manganites, dilute magnetic semiconductors, and some superconductors (*3*). In particular, the relaxor-based ferroelectrics PMN-*x*PT {$(1-x)[Pb(Mg_{1/3}Nb_{2/3})O_3] - xPbTiO_3$} and PZN-*x*PT {$(1-x)[Pb(Zn_{1/3}Nb_{2/3})O_3] - xPbTiO_3$} have electromechanical responses that are 10-fold larger than those of industry-standard PZT ($PbZrO_3$–$PbTiO_3$) piezoelectric ceramic materials (*1*, *4*) and have markedly improved technologies ranging from medical three-dimensional ultrasonography to sonar (*5*). The key features of the parent relaxor ferroelectrics, PMN and PZN, are inhomogeneous polar nanoregions (PNRs) (*6*–*9*), which have been invoked to explain their slow dielectric relaxation and diffuse phase transitions (*6*–*9*). However, with increasing PT, large domains form below the Curie temperature (T_C) (*7*), and the materials behave more like conventional ferroelectrics [for example, $Pb(Zr,Ti)O_3$ and $(K,Na)NbO_3$].

A morphotropic phase boundary (MPB) occurs in relaxor-based ferroelectrics, in which the structure changes from rhombohedral to tetragonal (x > 9% for PZN-*x*PT and x > 30% for PMN-*x*PT) (*10*). It is near this phase instability that the largest values for the electromechanical coupling occur (*4*, *10*–*13*). Peaks in the piezoelectric response occur near MPBs and polymorphic phase transitions in conventional ferroelectric materials [and even in a homogeneous ferroelectric with pressure-induced transition (*14*)], but none of these materials have the ultrahigh piezoelectric responses of relaxor-based ferroelectric crystals, which have longitudinal piezoelectric coefficients (d_{33}) that are >1500 pC/N and electromechanical coupling factors (k_{33}) that are ~0.9 (*4*). These findings suggest that relaxor features play an important role (*15*), although a portion of this enhanced response also comes from the fact that the relaxor-based ferroelectrics are single crystals. Xu *et al.* (*16*) found that PNRs are associated with phonon softening and argued that this may underlie the phase instability, but how PNRs soften phonons was not explained in their study.

More recently, it was shown that PNRs form by phonon localization (*17*) and that these localized phonons delocalize below T_C for compositions near the MPB (*17*). Phonon localization means that some phonons become trapped in small regions of the crystal and decouple from the spatially extended phonons. The localized modes have frequencies that are independent of wave vector (dispersionless), indicating that they are stationary (*17*). The underlying mechanism was attributed to Anderson localization (*17*), in which waves become trapped by a constructive interference effect on disorder-scattered waves (*18*). In this context, the static (or slow) atomic displacements of the PNRs are the average local distortions (local relaxation) associated with phonon localization that occurs at much higher frequencies. Anderson localization as a mechanism for PNR formation was also recently deduced from first-principle simulations (*19*) and theoretically derived from equations used to describe relaxor ferroelectric behavior (*20*). An earlier model explained PNRs in terms of intrinsic localized modes (*21*–*23*), in which nonlinearity is responsible for decoupling the local dynamics from the extended phonons. In this model, decoupling occurs because nonlinearity shifts the frequency of the local vibrations into a gap between modes, where they do not resonate with any of the extended modes (*24*). However, the observed localization occurs within the phonon bands and with characteristics matching those of Anderson localization (*17*). In either case, delocalization

[1]Materials Science and Technology Division, Oak Ridge National Laboratory, Oak Ridge, TN 37831, USA. [2]Quantum Condensed Matter Division, Oak Ridge National Laboratory, Oak Ridge, TN 37831, USA. [3]TRS Technologies, State College, PA 16801, USA. [4]NIST Center for Neutron Research, National Institute of Standards and Technology (NIST), Gaithersburg, MD 20899, USA.
*Corresponding author. Email: manleyme@ornl.gov
†Present address: Meggitt Sensing Systems, Irvine, CA 92606, USA.

occurs when these same modes develop dispersion as they couple to and move together with the spatially extended phonons, as hybrid modes.

Here, we demonstrate that the hybridization of the PNR local dynamics with transverse acoustic (TA) phonons results in shear softening that enables giant electromechanical coupling (*25*). The hybridization splits the TA mode into two phonons, one of lower frequency (softer) and one of higher frequency (stiffer), as compared to that of a bare acoustic phonon. The stiffer mode exhibits antisymmetric motion, meaning that the PNRs move out of phase with the phonon and it is the restoring force (coupling) between PNRs and the lattice that stiffens this mode. The softer mode exhibits symmetric motion, meaning that the PNRs move in phase with the phonon and this slows the mode down. This behavior is known as anticrossing or, sometimes, avoided crossing because of the way the hybrid modes appear to avoid each other in phonon dispersion relations (*26*). We also show that aligning the local modes and local structure in an electric field can enhance this phonon softening. In this way, the local vibrations of PNRs exert an enormous influence over the elastic shear stiffness, and this effect can be used to both understand and predict enhancements in the giant electromechanical response of relaxor-based ferroelectrics.

RESULTS

Neutron scattering on unpoled PMN-*x*PT

The neutron scattering intensity maps in Fig. 1 (A and B) show the phonon dispersion for unpoled PMN-30%PT above and below T_C. These time-of-flight neutron scattering maps show wave vectors along $Q = [2 + H, -2 + H, 0]$ for $0.0 < H < 0.4$, which preferentially selects for transverse phonons polarized along [1, −1, 0] and propagating along [1, 1, 0] [in the rhombohedral state below T_C, the coordinates refer to the pseudocubic unit cell, which is justified because different domains have zone centers shifted by less than 0.4% owing to the smallness of the lattice distortions (*27*)]. On cooling below T_C, the TA phonon splits into two branches. The splitting between these branches is about 1.5 meV at $H = 0.24$ (integrated over $H = [0.2, 0.28]$) (Fig. 1B, right). The intensity of the lower branch extends out to about $H = 0.24$ at an energy of 3 meV (Fig. 1B). Compared to the TA phonon above T_C (Fig. 1A), the upper branch is 0.6 meV higher at $H = 0.3$, whereas the lower branch is about 1 meV lower. The intensity of the lower branch extends out to about the same range as that of the PNR diffuse elastic scattering observed above T_C (*7*, *28*). Figure 1 (C and D) illustrates the behavior of the PNR diffuse scattering. Above T_C (Fig. 1C), the PNR diffuse scattering forms a lobe of intensity that extends out to about $H \approx 0.2$ (*7*), whereas below T_C (Fig. 1D), the diffuse scattering diminishes and the remaining intensity appears closer to the Bragg peak (*7*). This suggests that the PNR diffuse elastic intensity moves into the lattice dynamics on cooling below T_C. To further test this idea, we mapped the intensity of the lower TA phonon branch integrated over 3 ± 1 meV in the (*HK*0) plane (Fig. 1E). As can be seen by comparing Fig. 1E and Fig. 1C [after Matsuura *et al.* (7) and Xu *et al.* (28)], the intensity distribution of the lower branch closely resembles the lobe of PNR diffuse scattering above T_C, thus supporting the idea that PNR diffuse elastic scattering merges with lattice dynamics. A merging of PNR diffuse scattering with lattice dynamics is an expected consequence of coupling the slow PNR dynamics above T_C (*29*) to the lattice below T_C.

The simple model calculation shown in Fig. 2 illustrates how coupling a lattice to small localized clusters that represent PNRs (Fig. 2C) results in two TA-PNR hybrid modes (Fig. 2D). Details are provided in Supplementary calculations. This behavior is a general consequence of coupling modes that share a common frequency and can be understood in terms of anticrossing (*26*). Consider the two motions for the TA phonon and random PNRs illustrated in Fig. 2E. Without TA-PNR coupling, the PNR motion occurs independently of the bulk crystal phonon, and hence the frequencies for these two scenarios can be identical. With coupling, the frequencies of these two motions become different. In the antisymmetric mode, the coupling results in a restoring force between the PNR and the TA phonon displacements, which stiffen the collective motion. In the symmetric mode, the cooperative motion of the PNRs with the phonon increases the effective mass of the oscillation, and this lowers the frequency (*26*). The onset of coupling below T_C (Fig. 1) makes sense because the spontaneous polarization of the lattice engages coupling to PNRs through a dipole interaction. This is also consistent with the ~11.5-meV PNR local mode developing dispersion below T_C (*17*) because this dispersion also indicates a coupling to the lattice. Using triple-axis neutron scattering, we confirm that dispersion develops in the same way for PNR local modes in PZN-5%PT and PMN-38%PT, on cooling below T_C (see fig. S1). The absence of PNR coupling to the lattice above T_C is surprising but has been explained in terms of an Anderson-type phonon localization mechanism that occurs at higher frequencies (*17*–*20*), in which wave interference from disorder scattering effectively decouples local regions (*18*). However, as discussed in Neutron Scattering on Poled PMN-30%PT, there are multiple components to the PNR diffuse scattering, not all of which merge with the lattice dynamics, and the situation must be sorted out by poling the crystals (*30*).

Neutron scattering on poled PMN-30%PT

To explore the effects of poling on the TA-PNR mode hybridization, the ~11.5-meV PNR local mode (*17*), and the PNR diffuse elastic scattering, we electric field–poled a PMN-30%PT crystal along the [100] direction. The [100] poling direction is chosen here because the resulting 4R "engineered" domain structure elicits the largest piezoelectric response (*31*) (4R refers to the occurrence of just four of the eight <111>-type rhombohedral domains; that is, the four domains inclined toward the [100] poling axis).

Comparing Fig. 1B and Fig. 1F reveals the effect of [100] poling on the transverse [110] phonons. Upon poling, the [110]-TA phonon splitting increases from 1.5 meV (Fig. 1B) to 2 meV (Fig. 1F). This 2-meV splitting is also confirmed with an equivalent measurement in the (1, −1, 0) zone (Fig. 1G). The lower branch of the split TA mode also appears significantly softened near the zone center in the poled crystal, as compared to the unpoled crystal; the TA phonon at $H = 0.1$ softens from 3.2 to 2.2 meV (Fig. 1, B and F, left). Even closer to the zone center at $H = 0.05$, the [100]-poled crystal has a TA phonon peak that merges with the elastic line and appears four times more intense. The fourfold increase in intensity is consistent with a phonon frequency that is half the value because the scattering intensity of a phonon in the high temperature limit scales as the inverse square of the phonon frequency (*32*). Hence, the TA phonon splitting results in a lower branch that is softer by about a factor of 2, and this includes the long-wavelength modes occurring near the zone center ($H = 0$). According to the simple phonon model in Fig. 2, the increased splitting and shear mode softening are consistent with an increase in the effective mass of the PNRs carried by the TA-PNR mode, M_{PNR}. This suggests that poling results in a larger fraction of the PNRs being carried

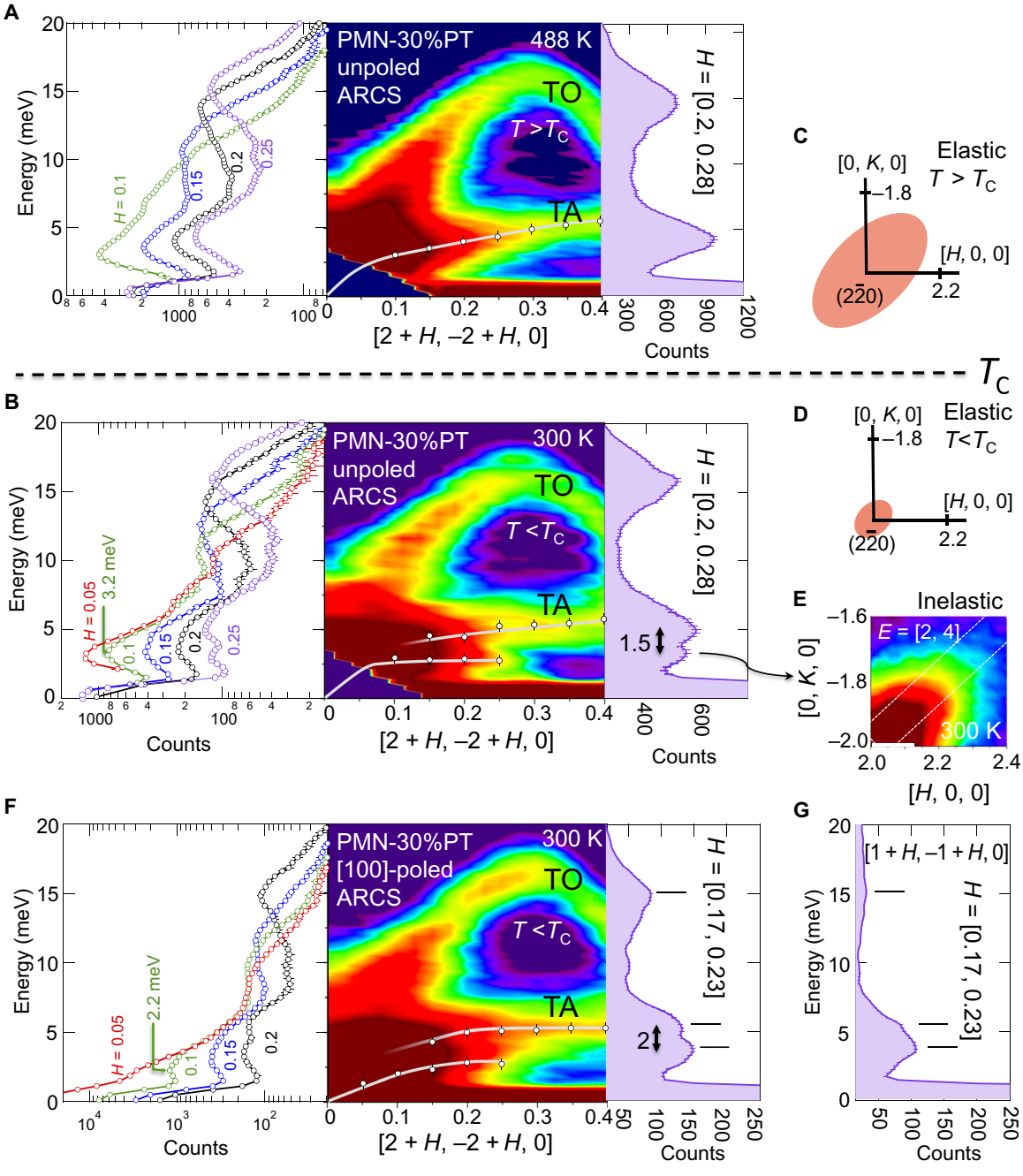

Fig. 1. Phonon dispersion along Q = [2 + H, –2 + H, 0] (L = 0 ± 0.05) in PMN-30%PT comparing temperature and poling effects. (**A**) Unpoled crystal measured above T_C at 488 K showing a single TA mode. (**B**) Unpoled crystal measured below T_C at 300 K showing splitting of the TA phonon. (**C** and **D**) Sketches of the diffuse elastic scattering around (*HH*0) reflections in the (*HK*0) plane, above and below T_C (*7*, *28*). (**E**) Inelastic scattering intensity map at the energy of the lower branch of the split TA phonon (E = [2, 4] meV) near the (2, –2, 0) reflection in the (*HK*0) plane. (**F**) [100]-poled PMN-30%PT showing a marked softening of the lower section of the TA branch (left) and an increase in the splitting of the TA mode from 1.5 to 2 meV (right). Data points overlaying the images of the TA phonon [center in (A), (B), and (F)] are peak positions from fits to the data, and the white lines running through these points are guides to the eye. (**G**) Confirmation of features in the (1, –1, 0) zone for the same direction, Q = [1 + H, –1 + H, 0]. The transverse optic (TO) and upper TA branch appear relatively weaker in the (1, –1, 0) zone, but the same features appear. All measurements were made on the time-of-flight angular-range chopper spectrometer (ARCS) at the Spallation Neutron Source, Oak Ridge National Laboratory.

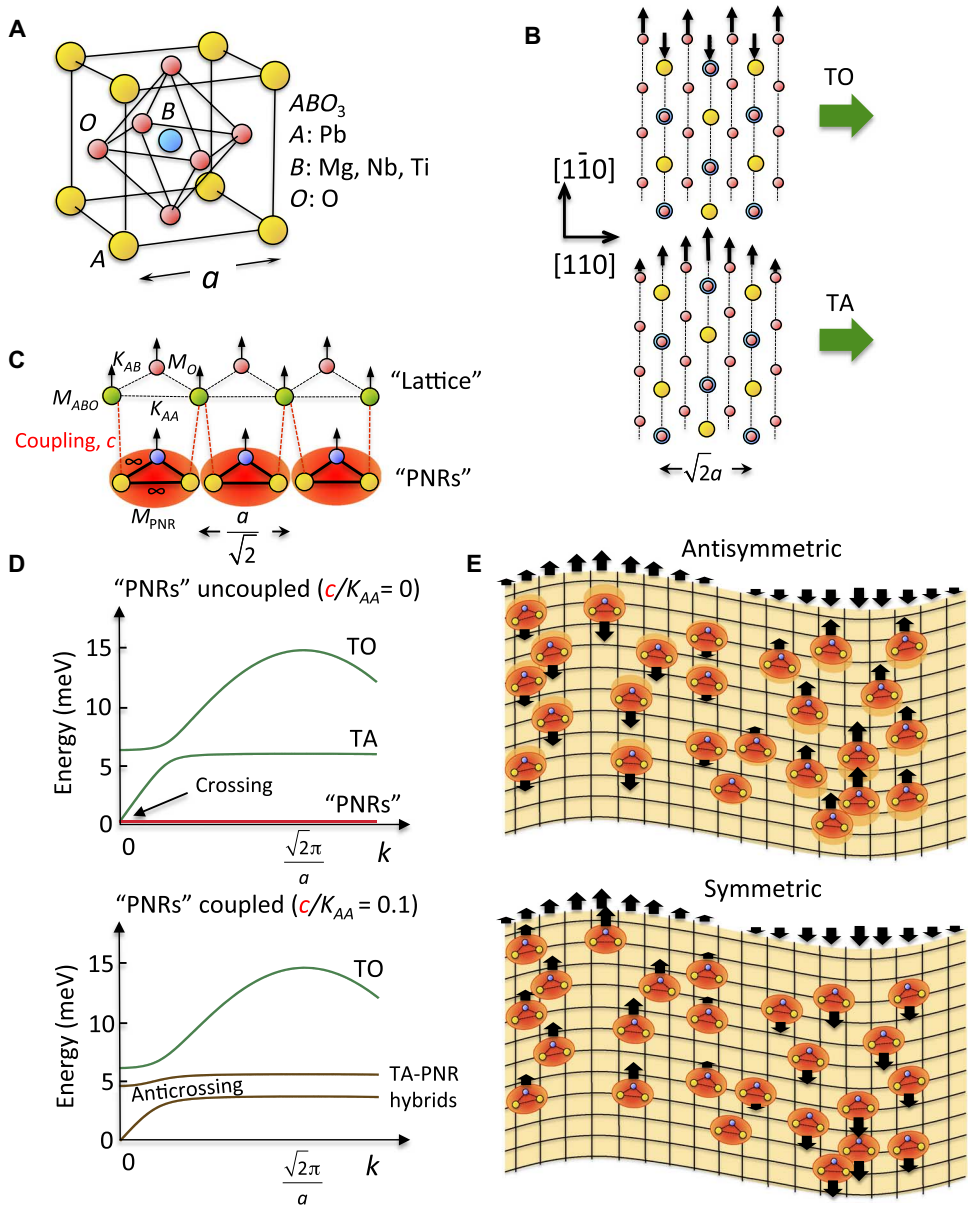

Fig. 2. Simple model for coupling lattice modes to PNRs. (**A**) Average crystal structure of PMN-PT. (**B**) The TO and TA phonons approximated as one-dimensional displacements of planes of atoms. (**C**) Model for coupling PNR clusters to the lattice, where M_O is the atomic mass of 2*O*, 32 u; M_{ABO} is the average mass on the alternate plane containing 1*A*, 1*B*, and 1*O* atoms, 286.4 u; and M_{PNR} is the fractional mass of the PNR clusters, 200 u (see Supplementary calculations). The force constants are K_{AA} = 14,000 u-meV^2 and K_{AO} = 500 u-meV^2. The PNRs are assumed to be internally rigid, and *c* accounts for the coupling between the lattice and PNRs. (**D**) The solution for zero coupling, c/K_{AA} = 0, exhibiting TO and TA modes and zero-energy PNR cluster dynamics that cross the TA mode at k = 0. Solution with coupling, c/K_{AA} = 0.1, exhibits anticrossing with low-energy dynamics. At k = 0, the lower symmetric branch has PNRs moving in phase, and the upper antisymmetric branch has them moving out of phase with the lattice. (**E**) Sketch of the symmetric and antisymmetric TA-PNR motions in a lattice partially occupied with PNRs.

in this TA-PNR mode. As discussed below, it is the softening of this same [110]-TA shear mode that enables the giant electromechanical response.

A direct alignment of the PNR local mode (*17*) polarization with the [100] poling direction is evidenced in Fig. 3 (A and B). Figure 3A shows measurements in a transverse geometry that selects for modes that displace atoms nearly parallel to the [100] poling direction (see schematic of scattering geometry in Fig. 3). In this direction, the PNR mode, between the TO mode and the TA mode near 11 meV, appears strongly enhanced; relative to the respective TO phonon intensities, the PNR mode is about three times more intense than that for the unpoled PMN-30%PT (*17*). There is also a hint of some splitting of the TA phonon in the cut integrated over $-0.5 < K < -0.4$, but this is difficult to resolve and is much weaker than that observed along the [110] direction (Fig. 1, B and F). The measurements in Fig. 3B are in a similar transverse geometry but select for modes that displace atoms

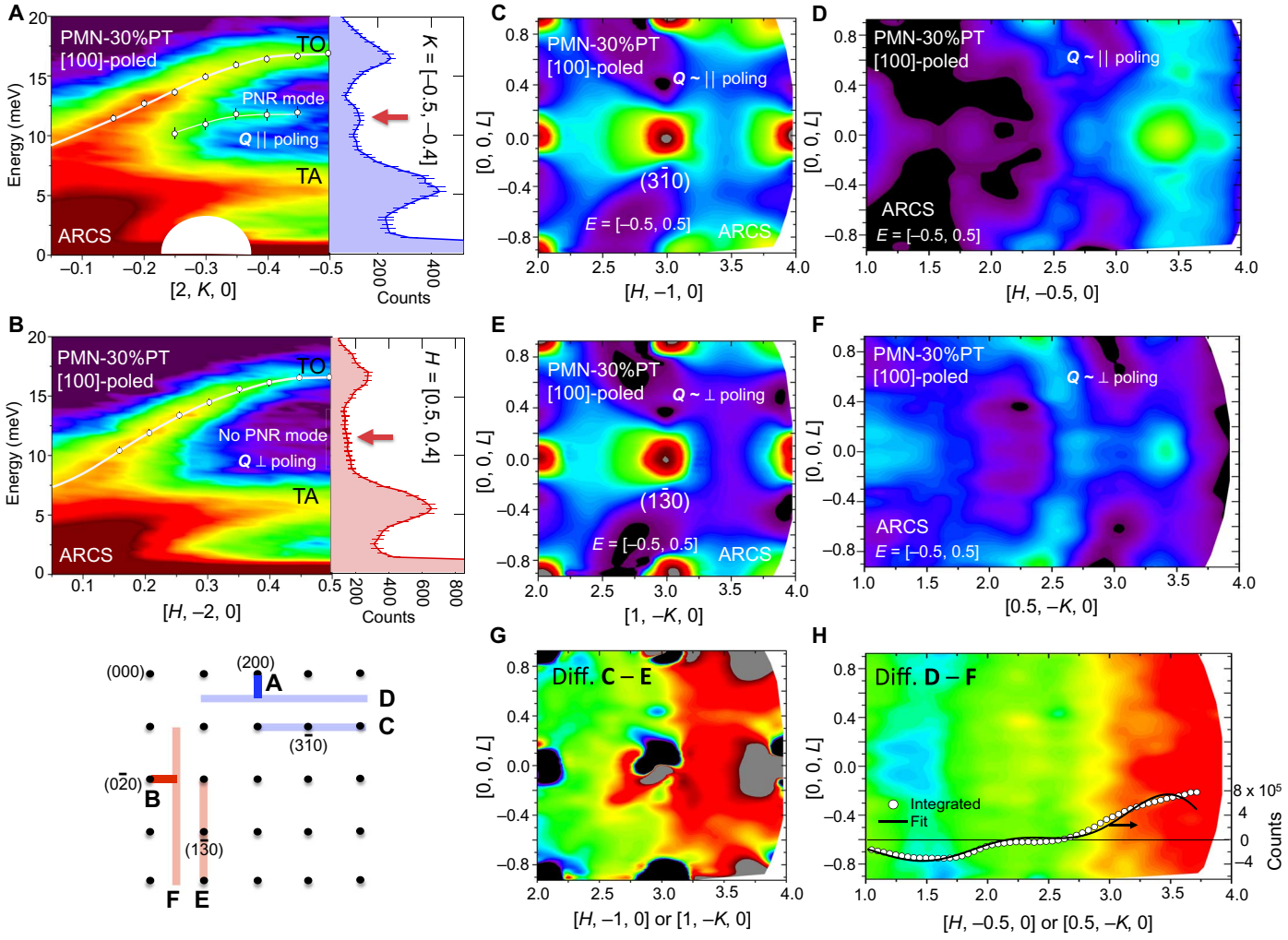

Fig. 3. Time-of-flight neutron scattering measurements of [100]-poled and unpoled PMN-30%PT at 300 K. (**A**) Phonon dispersion measured along Q = [2, K, 0] (H = 2 ± 0.025 and L = 0 ± 0.025). The PNR mode appears enhanced in this direction. (**B**) Phonon dispersion measured along Q = [H, −2, 0] (K = −2 ± 0.025 and L = 0±0.025). The PNR mode does not appear in this direction. The data points overlaying the images to the left of (A) and (B) are from peak fits, and the white lines running through these points are guides to the eye. (**C** and **D**) Diffuse elastic scattering (E = 0 ± 0.5 meV) measured with Q approximately parallel to the [100] poling direction on the (H, −1 ± 0.025, L) and (H, −0.5 ± 0.025, L) planes. (**E** and **F**) Diffuse elastic scattering on the (1 ± 0.025, K, L) and (0.5 ± 0.025, K, L) scattering planes, which are the equivalent to (C) and (D) except along directions approximately perpendicular to the [100] poling direction (see diagram for geometries). (**G** and **H**) Difference images created by subtracting (E) from (C), and (F) from (D) revealing vertical bands of diffuse scattering. The inset data points in (H) were obtained by integrating the difference image over L = [−1, 1]. The fit is described in the text. All measurements were made on the time-of-flight ARCS at the Spallation Neutron Source, Oak Ridge National Laboratory.

(nearly) perpendicular to the [100] poling direction. In this direction, the PNR modes are absent, and there is no evidence of splitting in the TA phonon peak. The dispersion in the TO phonon is also steeper without the PNR mode, falling ~2 meV lower near the zone center and not appearing as flat near the zone edge (Fig. 3, A and B). The flattening of the TO phonon in Fig. 3A can be understood as a repulsion between the TO phonon and the PNR mode (the flatter mode contributes a sharper and more intense TO peak to the integration cut). Together, these results show that the high-frequency PNR modes align with the [100] poling field and modify the TO phonon along the poling direction.

The PNR diffuse elastic scattering also appears altered parallel to the poling direction (Fig. 3, C and D), relative to the equivalent perpendicular directions (Fig. 3, E and F), indicating a rearrangement of static local displacements. The changes in diffuse scattering occur primarily in broad planes oriented perpendicular to the poling direction, whereas the more complex scattering around the Bragg peaks does not change, as seen in the difference images in Fig. 3 (G and H). The broad diffuse intensity integrated over L (inset to Fig. 3H) fits a profile

$$I_{[H,-0.5,0]} - I_{[0.5,-H,0]} = \alpha \times H^2 \cos\left(2\pi H(1/2)\right) + \beta \times \mathrm{H} \sin\left(2\pi H(1/2)\right) \quad (1)$$

and a monotonic background, where α and β are constants of the fit. This is a known solution for a crystal with additional well-defined local

displacements between atomic pairs separated by $a/2$ in the [100] poling direction (*33*). The decrease in the monotonic diffuse scattering indicates a corresponding decrease in local displacements occurring with random magnitudes.

There are two components of the diffuse scattering in relaxor-based ferroelectrics: a butterfly-shaped pattern that appears around Bragg peaks and the broader component described above. The former has been the focus of most previous studies of diffuse scattering in relaxor and relaxor-based ferroelectrics (*28*, *34*–*38*). Xu *et al.* (*39*) observed the latter in the scattering from [100]-poled PZN-4.5%PT, but the measurement did not cover enough reciprocal space to observe the broad modulations across Q space. Pair distribution function analysis of PMN powders indicates local Pb off-centering on this scale (*40*), but these studies did not include poling effects. Measurements of the local mode structure factor at high temperatures also indicate that well-localized modes first form near the Burns temperature and then drive the formation of the larger PNR structures (~2 nm) on cooling (*17*), which indicates that both components of the diffuse scattering are associated with the same PNRs. This is also supported by the fact that the poling-induced [100] local displacements (Fig. 3) also appear to modify the TA-PNR mode hybridization along the [110] direction (Fig. 1, B and F). The bulk rhombohedral domains do not rotate into the [100] direction but rather distort along the four <111>-type directions inclined toward the [100] poling direction, in the 4R domain structure (*31*). However, by applying a much larger electric field, it is possible to induce a phase transition to a single tetragonal domain poled along [100] (*1*). Hence, the PNR modes and local displacements are more easily aligned along the [100] poling direction than are the ferroelectric domains in which they are embedded, and this is expected because the ferroelectric domains are large, static, and pinned.

DISCUSSION

The observed shear mode softening (Fig. 1) is consistent with ultrasonic pulse echo measurements that show a soft shear acoustic mode along [110] in the (001) plane for [100]-poled PMN-33%PT (*41*); this is equivalent to the TA phonon in Fig. 1 at long wavelengths ($H \rightarrow 0$). A similar ultrasonic result was found for [100]-poled PZN-4.5%PT (*42*). In these studies, it was argued that the soft shear mode must result from domain motion induced by the ultrasound measurement (*42*). However, the phonon softening in Fig. 1 (B and F) shows that shear softening extends to wavelengths much shorter than the domain size. From the picture presented in Fig. 2E, we can understand that the softening originates from the increased effective mass felt by the symmetric mode because more PNRs couple to and move collectively with the TA phonon. A key point here is that the PNRs are smaller than a large share of the phonon wavelengths, and for this reason, they manifest in a way that is more akin to an impurity mode (*43*) than to a macroscopic domain.

The TA phonon softening (Fig. 1) is also reminiscent of the softening observed using neutron scattering in [111]-poled single-domain PZN-4.5%PT for the same TA mode: it is the phonons that are aligned with PNR diffuse scattering patterns that soften (*16*). However, in these measurements, neither the PNR vibrational modes (*17*) nor the anticrossing of the phonons (Fig. 1) was detected. These features were easily missed because the ~0.3-cm^3 crystal used in a previous study (*16*) was about 60 times smaller than the ~20-cm^3 crystals used here (fig. S2). With this knowledge, we can now understand that the relationship between PNRs and phonon softening described by Xu *et al.* (*16*) likely originates from the hybridization of the PNRs with the TA phonon (Figs. 1 and 2).

The shear softening induced by [100] poling (Fig. 1F) directly relates to the ease of the polarization rotations (*25*) underlying the giant

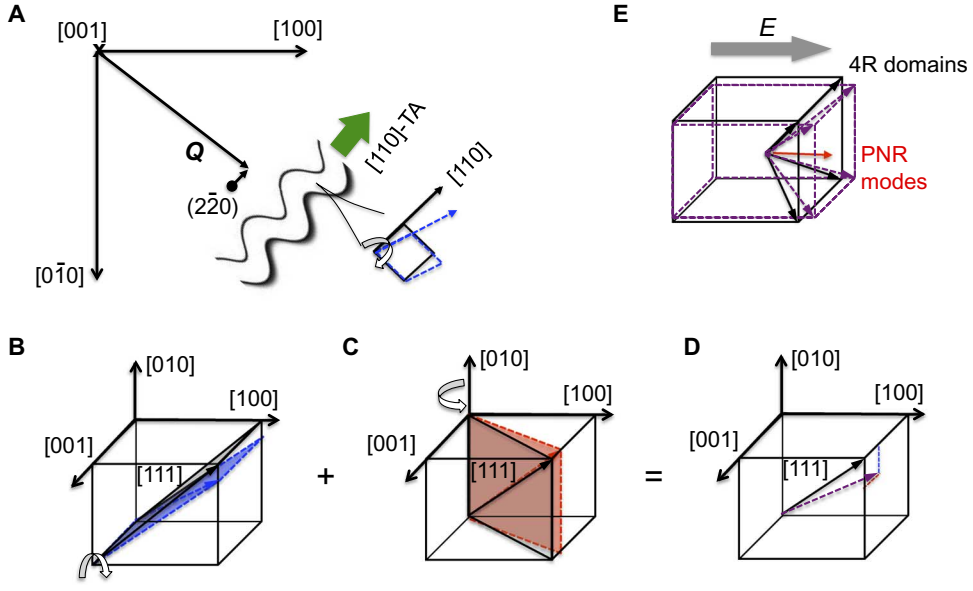

Fig. 4. Relationship between the soft [110]-TA phonon and the giant electromechanical coupling. (**A**) The [110]-TA phonon displacements include a shear deformation that tilts the [110] axis around the nonpolar [001] axis. The softening of this phonon at long wavelengths (near the zone center in Fig. 1) implies a softening of the indicated shear distortion. (**B**) The tilting of the [110] axis around [001] also results in the tilting of the [111] axis around [001] because it is in the same tilting plane [the (1, −1, 0) plane]. (**C**) An equivalent soft TA phonon involving the tilting of the [111] axis around [010] (the other nonpolar axis) must also exist by symmetry. (**D**) Combination of the soft distortions in (B) and (C) rotates the [111] axis toward the [100] polar axis. (**E**) Equivalent distortions in all four rhombohedral domain variants (4R) (*31*) distort the domains toward the [100] poling direction under the application of an electric field, E. The [100] poling aligns the PNR modes along the poling direction (red arrow).

electromechanical coupling used in applications (*4*). The high longitudinal piezoelectric coefficients along the poling axis for the [100]-poled 4R engineered domain (*31*) state are attributed to a high-shear piezoelectric response in the single domain state (*4*, *44*–*47*). This is because the polarization rotations involve shearing of the individual domains (*1*). Figure 4 illustrates how the softening of the [110]-TA phonons observed in Fig. 1 implies a softening of these shear deformations. The soft shear mode (Fig. 4A) makes it easy to tilt the [111] axis about [001] (Fig. 4B), whereas an equivalent soft shear makes it easy to tilt about [010] (Fig. 4C). Together, the [111] axis is easy to tilt toward the [100] poling axis (Fig. 4D), and the same argument applies to all 4R domains. The result is the large piezoelectric response along the [100] poling direction (Fig. 4E). The alignment of the PNR modes acts synergistically with the intrinsic effect of being near the MPB to lower the energy barriers of the polarization rotations (*25*) because the MPB occurs even without PNR mode alignment. Pirc *et al.* (*48*) proposed a semimicroscopic model for PNR-enhanced electromechanical coupling, in which the interactions between PNRs are explained in terms of a dipole-phonon interaction. However, the effect coupling the phonons to the PNR vibrations, which underlies the anticrossing-induced shear softening, was not considered.

Our results reveal that domain engineering of relaxor-based ferroelectric single crystals (*31*) enhances the electromechanical coupling for two reasons, one deliberate and one serendipitous. Whereas the deliberate 4R arrangement of the domains mechanically facilitates the conversion of the high-shear piezoelectric response into a longitudinal response (*31*), the serendipitous alignment of the PNR vibrational modes and local structure (Fig. 3) further enhances this shear response by softening the TA phonon through the anticrossing (Fig. 1F). This engineered phonon softening was likely missed as a contribution in bulk measurements (*4*) because single-domain <111>-poled crystals used for comparison also have TA phonons that are softened by having the PNR modes aligned during the poling process (*16*). However, the underlying cause is important to recognize because an optimally engineered relaxor-based ferroelectric crystal should enhance both the domain mechanics (*31*) and the appropriate shear softening (*4*) to maximize the electromechanical coupling. In this context, the high-frequency PNR vibrational modes fully align with the [100] poling field (Fig. 3), whereas the larger domains remain in the 4R configuration unless much larger fields are applied (*1*). This suggests that it should be possible to independently engineer the domain structure and the local structure or dynamics, optimizing each to improve performance.

Our work establishes the crucial role that nanoregion local vibrations play in the performance of relaxor-based ferroelectrics and reveals an elastic softening mechanism that is likely applicable to other nanostructured materials. For example, ferroelastic nanoregions might enable the superelasticity of shape-memory strain glass alloys (*2*) by inducing similar elastic softening. Thus, our work provides a new perspective for understanding and controlling the performance of nanostructured materials.

MATERIALS AND METHODS

Time-of-flight inelastic neutron scattering

Time-of-flight measurements were performed on a large (~20 cm^3) [100]-poled PMN-30%PT crystal (see fig. S2 for pictures of crystal) and, for comparison, an unpoled PMN-30%PT crystal (~10 cm^3) using the ARCS at the Spallation Neutron Source, Oak Ridge National Laboratory (*49*). All measurements were performed with the crystals oriented in the (*HK*0) plane and with an incident neutron energy of 25 meV. Comprehensive four-dimensional *Q*-*E* volumes of data were obtained by rotating the angle between the [100] axis and the incident beam in 0.5° steps and combining the data using Mslice in the DAVE (Data Analysis and Visualization Environment) software (*50*). For the unpoled PMN-30%PT crystal, data were collected at each angle from 0° to 60°. For the poled PMN-30%PT crystal, data were collected at each angle from −70° to 55° to obtain a complete data set that includes *Q* values in directions both perpendicular and parallel to the [100] poling direction in the (*HK*0) plane.

Triple-axis inelastic neutron scattering

Large (~10 cm^3) single crystals of PZN-5%PT and PMN-38%PT were measured using triple-axis neutron spectroscopy. The PMN-38%PT crystal was measured on the BT7 spectrometer at the National Institute of Standards and Technology Center for Neutron Research (*51*). The spectrometer was operated with a filtered fixed final neutron energy of 13.7 meV [with horizontal collimation of 120′:50′:50′:120′ (*32*)], and the crystals were mounted in a furnace with the (*HK*0) reflections in the scattering plane using a vanadium holder (vanadium was used because it scatters incoherently). Measurements were made along [2, *K*, 0] at 21 equally spaced values of *K* between 0 and 0.5 at temperatures above and below T_C: 515 and 300 K for PMN-38%PT (T_C = 465 K). The PZN-5%PT crystal, also mounted in a vanadium holder, was measured on the HB3 spectrometer at the High Flux Isotope Reactor at Oak Ridge National Laboratory. The HB3 spectrometer was operated with a filtered fixed final neutron energy of 14.7 meV (with horizontal collimation of 48′:60′:80′:120′), and measurements were made with the same crystal orientation and at the same points in reciprocal space as with BT7, again at temperatures above and below T_C: 500 and 300 K (T_C = 425 K for PZN-5%PT). Both instruments used pyrolytic graphite PG(002) for the monochromator and the analyzer.

Crystal growth and electric field poling

PMN-PT single-crystal boules were grown using a modified Bridgman growth method. The boules were oriented for the major crystallographic orientations $[001]_c$, $[011]_c$, and $[111]_c$ using Laue x-ray and x-ray diffractometry. Sections of crystals 0.5 cm thick were sliced from the boule using an ID (inner diameter) saw. The composition of the crystals was first estimated from the positions in the crystal boules and then later confirmed by measuring the transition temperatures using high-temperature x-ray diffraction on the individual crystals and comparing these to the known phase diagrams. For the unpoled PMN-30%PT crystals, the slices were used as cut.

For poling purposes, two slices (0.5 cm thick and ~5 cm in diameter) were cleaned and metallized with chromium (~500-Å layer) and gold (2000-Å layer) using a sputtering process (fig. S2). The metallized section was then poled using a polarization bath. The crystal slice was immersed in a bath of Fluorinert oil (silicone oil with high dielectric strength), and a dc electric field was applied. For the rhombohedral PMN-30%PT crystal, the crystal samples were poled by applying a dc electric field of 4 kV/cm at room temperature. Piezoelectric charge coefficient (d_{33}) was measured using a d_{33} meter to determine whether the crystal slices were poled into a piezoelectric state. After poling, polarization changes (as a function of applied electric field) were observed on batch qualification samples using a hysteresis loop device that works

based on the Sawyer-Tower circuit. This measurement uses an integrator to determine the charge per unit area formed on the electrode surface of a dielectric subjected to an electric field. The voltage is applied in the form of a biased (unipolar) triangle wave (0 to peak) for a small number of cycles (~3). The hysteresis area between the field-ascending and the field-descending portions of the curve is proportional to the energy lost as heat during a charge-discharge cycle, and this hysteresis loop represents a behavior that is typical of ferroelectric materials.

SUPPLEMENTARY MATERIALS

Supplementary material for this article is available at http://advances.sciencemag.org/cgi/content/full/2/9/e1501814/DC1

Supplementary calculations

fig. S1. Phonon dispersion curves measured along Q = [2, K, 0] in PZN-5%PT and PMN-38%PT, both above and below T_C.

fig. S2. Photograph of poled PMN-30%PT crystals.

References (*52*, *53*)

REFERENCES AND NOTES

1. S.-E. Park, T. R. Shrout, Ultrahigh strain and piezoelectric behavior in relaxor based ferroelectric single crystals. *J. Appl. Phys.* **82**, 1804–1811 (1997).
2. Y. Wang, X. Ren, K. Otsuka, Shape memory effect and superelasticity in a strain glass alloy. *Phys. Rev. Lett.* **97**, 225703 (2006).
3. E. Dagotto, Complexity in strongly correlated electronic systems. *Science* **309**, 257–262 (2005).
4. S. Zhang, F. Li, High performance ferroelectric relaxor-$PbTiO_3$ single crystals: Status and perspective. *J. Appl. Phys.* **111**, 031301 (2012).
5. K. Uchino, *Piezoelectric Actuators and Ultrasonic Motors* (Kluwer Academic Publishers, Dordrecht, 1996).
6. G. Burns, F. H. Dacol, Crystalline ferroelectrics with glassy polarization behavior. *Phys. Rev. B* **28**, 2527–2530 (1983).
7. M. Matsuura, K. Hirota, P. M. Gehring, Z.-G. Ye, W. Chen, G. Shirane, Composition dependence of the diffuse scattering in the relaxor ferroelectric compound $(1-x)Pb(Mg_{1/3}Nb_{2/3})O_3$–$xPbTiO_3$($0<x<0.40$). *Phys. Rev. B* **74**, 144107 (2006).
8. R. Blinc, V. Laguta, B. Zalar, Field cooled and zero field cooled ^{207}Pb NMR and the local structure of relaxor $PbMg_{1/3}Nb_{2/3}O_3$. *Phys. Rev. Lett.* **91**, 247601 (2003).
9. V. V. Shvartsman, A. L. Kholkin, Domain structure of $0.8Pb(Mg_{1/3}Nb_{2/3})$–$0.2PbTiO_3$ studied by piezoresponse force microscopy. *Phys. Rev. B* **69**, 014102 (2004).
10. Y. Guo, H. Luo, D. Ling, H. Xu, T. He, Z. Yin, The phase transition sequence and the location of the morphotropic phase boundary region in $(1-x)[Pb(Mg_{1/3}Nb_{2/3})O_3]$–$xPbTiO_3$ single crystal. *J. Phys. Condens. Matter* **15**, L77–L82 (2003).
11. J. Tian, P. Han, D. A. Payne, Measurements along the growth direction of PMN-PT crystals: Dielectric, piezoelectric, and elastic properties. *IEEE Trans. Ultrason. Ferroelectr. Freq. Control* **54**, 1895–1902 (2007).
12. F. Li, S. Zhang, Z. Xu, X. Wei, J. Luo, T. R. Shrout, Composition and phase dependence of the intrinsic and extrinsic piezoelectric activity of domain engineered $(1–x)Pb(Mg_{1/3}Nm_{2/3})O_3$–$xPbTiO_3$ crystals. *J. Appl. Phys.* **108**, 034106 (2010).
13. Z. Kutnjak, J. Petzelt, R. Blinc, The giant electromechanical response of ferroelectric relaxors as a critical phenomenon. *Nature* **441**, 956–959 (2006).
14. M. Ahart, M. Somayazulu, R. E. Cohen, P. Ganesh, P. Dera, H.-k. Mao, R. J. Hemley, Y. Ren, P. Liermann, Z. Wu, Origin of morphotropic phase boundaries in ferroelectrics. *Nature* **451**, 545–548 (2008).
15. D. Phelan, C. Stock, J. A. Rodriguez-Rivera, S. Chi, J. Leão, X. Long, Y. Xie, A. A. Bokov, Z.-G. Ye, P. Ganesh, P. M. Gehring, Role of random electric fields in relaxors. *Proc. Natl. Acad. Sci. U.S.A.* **111**, 1754–1759 (2014).
16. G. Xu, J. Wen, C. Stock, P. M. Gehring, Phase instability induced by polar nanoregions in a relaxor ferroelectric system. *Nat. Mater.* **7**, 562–566 (2008).
17. M. E. Manley, J. W. Lynn, D. L. Abernathy, E. D. Specht, O. Delaire, A. R. Bishop, R. Sahul, J. D. Budai, Phonon localization drives polar nanoregions in a relaxor ferroelectric. *Nat. Commun.* **5**, 3683 (2014).
18. A. Lagendijk, B. van Tiggelen, D. S. Wiersma, Fifty years of Anderson localization. *Phys. Today* **62**, 24–29 (2009).
19. A. R. Akbarzadeh, S. Prosandeev, E. J. Walter, A. Al-Barakaty, L. Bellaiche, Finite-temperature properties of $Ba(Zr, Ti)O_3$ relaxors from first principles. *Phys. Rev. Lett.* **108**, 257601 (2012).
20. D. Sherrington, BZT: A soft pseudospin glass. *Phys. Rev. Lett.* **111**, 227601 (2013).
21. A. Bussmann-Holder, A. R. Bishop, T. Egami, Relaxor ferroelectrics and intrinsic inhomogeneity. *Europhys. Lett.* **71**, 249–255 (2005).
22. A. R. Bishop, A. Bussmann-Holder, S. Kamba, M. Maglione, Common characteristics of displacive and relaxor ferroelectrics. *Phys. Rev. B* **81**, 064106 (2010).
23. J. Macutkevic, J. Banys, A. Bussmann-Holder, A. R. Bishop, Origin of polar nanoregions in relaxor ferroelectrics: Nonlinearity, discrete breather formation, and charge transfer. *Phys. Rev. B* **83**, 184301 (2011).
24. D. K. Campbell, S. Flach, Y. S. Kivshar, Localizing energy through nonlinearity and discreteness. *Phys. Today* **57**, 43–49 (2004).
25. H. Fu, R. E. Cohen, Polarization rotation mechanism for ultrahigh electromechanical response in single-crystal piezoelectrics. *Nature* **403**, 281–283 (2000).
26. B. Skinner, "There's nothing particularly "spooky" about avoided crossing," http://gravityandlevity.wordpress.com/2014/04/08/avoided-crossing/ [accessed May 2016].
27. B. Noheda, Structure and high-piezoelectricity in lead oxide solid solutions. *Curr. Opin. Solid State Mater. Sci.* **6**, 27–34 (2002).
28. G. Xu, Z. Zhong, H. Hiraka, G. Shirane, Three-dimensional mapping of diffuse scattering in $Pb(Zn_{1/3}Nb_{2/3})O_3$–$xPbTiO_3$. *Phys. Rev. B* **70**, 174109 (2004).
29. H. Hiraka, S.-H. Lee, P. M. Gehring, G. Xu, G. Shirane, Cold neutron study on the diffuse scattering and phonon excitations in the relaxor $Pb(Mg_{1/3}Nb_{2/3})O_3$. *Phys. Rev. B* **70**, 184105 (2004).
30. G. Xu, Z. Zhong, Y. Bing, Z.-G. Ye, G. Shirane, Electric-field-induced redistribution of polar nano-regions in a relaxor ferroelectric. *Nat. Mater.* **5**, 134–140 (2006).
31. M. Davis, D. Damjanovic, D. Hayem, N. Setter, Domain engineering of the transverse piezoelectric coefficient in perovskite ferroelectrics. *J. Appl. Phys.* **98**, 014102 (2005).
32. G. Shirane, S. M. Shapiro, J. M. Tranquada, *Neutron Scattering with a Triple-axis Spectrometer: Basic Techniques* (Cambridge Univ. Press, Cambridge, 2002), p. 28.
33. J. M. Cowley, *Diffraction Physics* (North-Holland Physics, Amsterdam, 1975), p. 260.
34. A. Cervellino, S. N. Gvasaliya, O. Zaharko, B. Roessli, G. M. Rotaru, R. A. Cowley, S. G. Lushnikov, T. A. Shaplygina, M. T. Fernandez-Diaz, Diffuse scattering from the lead-based relaxor ferroelectric $PbMg_{1/3}Ta_{2/3}O_3$. *J. Appl. Crystallogr.* **44**, 603–609 (2011).
35. T. R. Welberry, D. J. Goossens, M. J. Gutmann, Chemical origin of nanoscale polar domains in $PbZn_{1/3}Nb_{2/3}O_3$. *Phys. Rev. B* **74**, 224108 (2006).
36. M. Paściak, M. Wocyrz, A. Pietraszko, Interpretation of the diffuse scattering in Pb-based relaxor ferroelectrics in terms of three-dimensional nanodomains of the ⊠110⊠-directed relative interdomain atomic shifts. *Phys. Rev. B* **76**, 014117 (2007).
37. P. Ganesh, E. Cockayne, M. Ahart, R. E. Cohen, B. Burton, R. J. Hemley, Y. Ren, W. Yang, Z.-G. Ye, Origin of diffuse scattering in relaxor ferroelectrics. *Phys. Rev. B* **81**, 144102 (2010).
38. A. Bosak, D. Chernyshov, S. Vakhrushev, M. Krisch, Diffuse scattering in relaxor ferroelectrics: True three-dimensional mapping, experimental artifacts and modelling. *Acta Crystallogr. Sect. A Found. Crystallogr.* **68**, 117–123 (2012).
39. Z. Xu, J. Wen, G. Xu, C. Stock, J. S. Gardner, P. M. Gehring, Two-component model of the neutron diffuse scattering in the relaxor ferroelectric PZN-4.5%PT. *Phys. Rev. B* **82**, 134124 (2010).
40. T. Egami, S. J. L. Billinge, *Underneath the Bragg Peaks: Structural Analysis of Complex Materials*, R. W. Cahn, Ed. (Pergamon Materials Series, Oxford, 2003), p. 343.
41. R. Zhang, B. Jiang, W. W. Cao, Elastic, piezoelectric, and dielectric properties of multidomain $0.67Pb(Mg_{1/3}Nb_{2/3})O_3$–$0.33PbTiO_3$ single crystals. *J. Appl. Phys.* **90**, 3471 (2001).
42. J. H. Yin, B. Jiang, W. W. Cao, Elastic, piezoelectric, and dielectric properties of $0.955Pb(Zn_{1/3}Nb_{2/3})O_3$–$0.045PbTiO_3$ single crystal with designed multidomains. *IEEE Trans. Ultrason. Ferroelect. Freq. Contr.* **47**, 285–291 (2000).
43. O. Delaire, I. I. Al-Qasir, A. F. May, C. W. Li, B. C. Sales, J. L. Niedziela, J. Ma, M. Matsuda, D. L. Abernathy, T. Berlijn, Heavy-impurity resonance, hybridization, and phonon spectral functions in $Fe_{1-x}M_xSi$ (M = Ir, Os). *Phys. Rev. B* **91**, 094307 (2015).
44. L. Bellaiche, A. García, D. Vanderbilt, Electric-field induced polarization paths in $Pb(Zr_{1-x}Ti_x)O_3$ alloys. *Phys. Rev. B* **64**, 060103 (2001).
45. M. Davis, M. Budimir, D. Damjanovic, N. Setter, Rotator and extender ferroelectrics: Importance of the shear coefficient to the piezoelectric properties of domain-engineered crystals and ceramics. *J. Appl. Phys.* **101**, 054112 (2007).
46. D. Damjanovic, Comments on origins of enhanced piezoelectric properties in ferroelectrics. *IEEE Trans. Ultrason. Ferroelectr. Freq. Control* **56**, 1574–1585 (2009).
47. E. Sun, W. Cao, Relaxor-based ferroelectric single crystals: Growth, domain engineering, characterization and applications. *Prog. Mater. Sci.* **65**, 124–210 (2014).
48. R. Pirc, R. Blinc, V. S. Vikhnin, Effect of polar nanoregions on giant electrostriction and piezoelectricity in relaxor ferroelectrics. *Phys. Rev. B* **69**, 212105 (2004).
49. D. L. Abernathy, M. B. Stone, M. J. Loguillo, M. S. Lucas, O. Delaire, X. Tang, J. Y. Y. Lin, B. Fultz, Design and operation of the wide angular-range chopper spectrometer ARCS at the Spallation Neutron Source. *Rev. Sci. Instrum.* **83**, 015114 (2012).
50. R. T. Azuah, L. R. Kneller, Y. Qiu, P. W. W. Tegenna-Piggott, C. M. Brown, J. R. D. Copley, R. M. Dimeo, DAVE: A comprehensive software suite for the reduction, visualization, and analysis of low energy neutron spectroscopic data. *J. Res. Natl. Inst. Stand. Technol.* **114**, 341–358 (2009).

51. J. W. Lynn, Y. Chen, S. Chang, Y. Zhao, S. Chi, W. Ratcliff II, B. G. Ueland, R. W. Erwin, Double-focusing thermal triple-axis spectrometer at the NCNR. *J. Res. Natl. Inst. Stand. Technol.* **117**, 61–79 (2012).
52. C. Kittel, *Introduction to Solid State Physics* (John Wiley & Sons Inc., ed. 7, New York, 1996).
53. A. A. Maradudin, E. W. Montroll, G. H. Weiss, *Theory of Lattice Dynamics in the Harmonic Approximation* (Academic Press, Cambridge, MA, 1963).

Acknowledgments: M.E.M. acknowledges useful communications with P. M. Gehring. **Funding:** This work was sponsored by the Office of Basic Energy Sciences, Materials Sciences and Engineering Division, U.S. Department of Energy. The portions of this research performed at the Oak Ridge National Laboratory's Spallation Neutron Source and High Flux Isotope Reactor facilities were sponsored by the Office of Basic Energy Sciences, U.S. Department of Energy. We acknowledge the support of the National Institute of Standards and Technology, U.S. Department of Commerce, in providing neutron research facilities used in this work. The identification of any commercial product or trade name does not imply endorsement or recommendation by the National Institute of Standards and Technology. **Author contributions:** M.E.M. conceived the experiments. D.L.A., M.E.M., J.D.B., and P.J.S. performed the time-of-flight neutron scattering measurements. M.E.M., D.E.P., J.W.L., and A.D.C. performed the triple-axis neutron scattering measurements. M.E.M. analyzed all neutron scattering data. E.D.S. performed the x-ray characterization of the single crystals. R.S. grew the single crystals and performed the electric field poling of the single crystals. M.E.M. wrote the manuscript with input from all authors. **Competing interests:** The authors declare that they have no competing interests. **Data and materials availability:** All data needed to evaluate the conclusions in the paper are included in the paper and/or the Supplementary Materials. Additional data related to this paper may be requested from M.E.M. (manleyme@ornl.gov).

Submitted 28 January 2016
Accepted 10 August 2016
Published 16 September 2016
10.1126/sciadv.1501814

Citation: M. E. Manley, D. L. Abernathy, R. Sahul, D. E. Parshall, J. W. Lynn, A. D. Christianson, P. J. Stonaha, E. D. Specht, J. D. Budai, Giant electromechanical coupling of relaxor ferroelectrics controlled by polar nanoregion vibrations. *Sci. Adv.* **2**, e1501814 (2016).